Small Structures

small structures

www.small-structures.com

RESEARCH ARTICLE OPEN ACCESS

Effect of Temperature Ramp in Rapid Folding of 3D DNA Origami Structures

Anurit Dey[1] | Mohammed Mustafa A. Al Hussain[1] | Xuan-Hung Pham[1] | Jacky Loo[1] | Ashwin Karthick Natarajan[1,2] | Anton Kuzyk[1]

[1]Department of Neuroscience and Biomedical Engineering, Aalto University, Espoo, Finland | [2]Structural Biology of Membrane-Associated Processes, Max-Delbrück-Center for Molecular Medicine in the Helmholtz Association (MDC), Berlin, Germany

Correspondence: Anton Kuzyk (anton.kuzyk@aalto.fi)

Received: 28 September 2025 | **Revised:** 15 November 2025 | **Accepted:** 24 November 2025

Keywords: assembly yield | DNA origami | self-assembly | temperature ramp

ABSTRACT

DNA origami (DO) has emerged as a powerful technique for constructing nanoscale structures and devices. However, conventional folding protocols for complex 3D DO structures are slow, typically requiring 24 h or longer, limiting scalability for practical applications. Here, we investigate the role of the temperature ramp in DO folding and propose a modified protocol that confines annealing to a 60°C–40°C window. Using four distinct designs, a 20-helix square box, a 24-helix bundle, a 13-helix ring, and a switchable cross structure, we evaluate folding yield, structural uniformity, and functional performance across a range of folding times and buffer conditions. We find that folding occurs rapidly within the 60°C–40°C window, with over 85% of the yield of the conventional 30 h protocol achieved within 1–3 h. Functional switching of the cross structure is retained even in samples folded in 30 min. For aggregation-prone structures, such as the 13-ring, the shorter ramp reduces multimer formation and improves the usable yield compared to prolonged folding. These findings confirm the critical influence of the temperature ramp in DO assembly and provide a broadly applicable protocol for faster folding, with potential impact in rapid prototyping, screening, and applications such as plasmonics, sensing, lithography, and metamaterials.

1 | Introduction

DNA nanotechnology is a branch of nanoscience that uses DNA molecules as programable building blocks to construct precisely defined structures and devices at the nanoscale [1–3]. One of the most promising methods in DNA nanotechnology is DNA origami (DO), where a long, single-stranded DNA strand, known as a "scaffold", is folded into specific 2D or 3D shapes with the assistance of hundreds of shorter DNA strands, referred to as "staples", which bind to the scaffold through the Watson–Crick–Franklin base pairing [4–6]. The DO technique enables the fabrication of highly customizable nanostructures with high spatial precision [5]. Due to their biocompatibility [7, 8], and programable functionalization [3], DO structures have been applied in diverse fields such as drug delivery [7–9], biosensing [10–12], plasmonics and nanophotonics [13–15], surface and interface functionalization [16–18], metamaterials [7, 19–21], molecular robotics [9, 22–24], and therapeutics [25]. The ability to design and manipulate matter at the molecular level positions DO as a foundational platform for next-generation nanomaterials [26–29], biomedical devices [30], and nanofabrication technologies [31].

The DO folding process typically begins by mixing the scaffold and staple strands in a buffer solution containing positive ions (cations), which stabilize the assembled DNA nanostructures (Figure 1A). This mixture is then typically subjected to a thermal annealing ramp, during which the scaffold-and-staples solution is gradually cooled from a temperature above DNA's melting point to room temperature [32]. This cooling step allows the staple strands to hybridize accurately with the scaffold and fold it into the desired configuration. For complex 3D structures, typical reported annealing times vary between 20 and 30 h [5, 32].

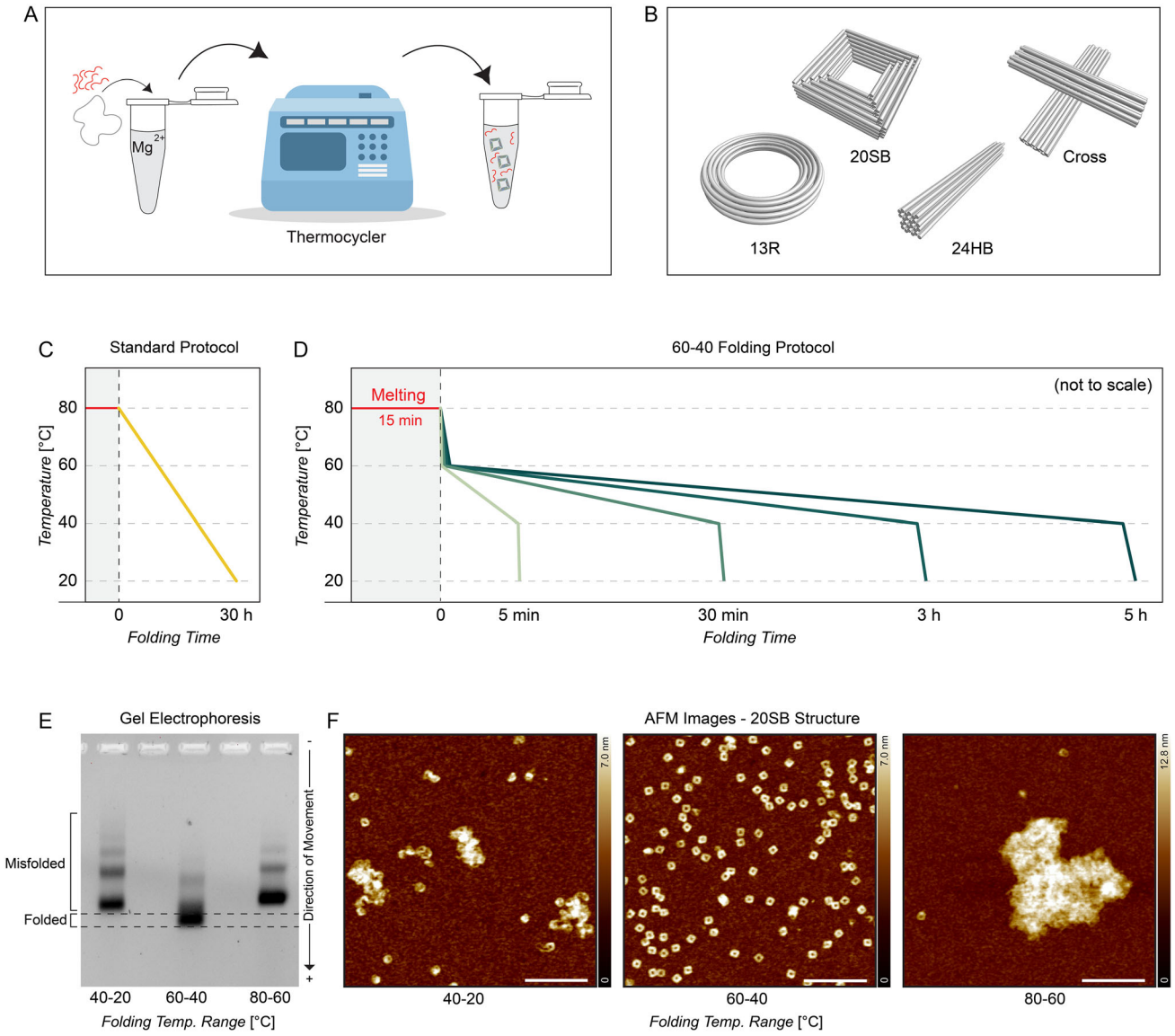

FIGURE 1 | (A) An illustration of the DO folding process. (B) A schematic illustration of the DO structures characterized in this study. (C) Typical DO folding temperature ramp. (D) The proposed 60–40 temperature ramp with different reaction times. (E) Gel electrophoresis image of 20SB DO structures folded for 30 min within the indicated temperature range (reaction time is negligible outside the temperature range mentioned). (F) Corresponding AFM images of 20SB DO structures folded within the indicated temperature range. Scale bars: 400 nm.

Historically, researchers have used annealing times as long as 1–2 weeks [32, 33]. While considerable research has focused on understanding the influence of design parameters [34–36], salt concentration [37–42], solvent [43], and buffer composition [43, 44] on folding efficiency, relatively few studies have investigated the role of the temperature ramp itself or strategies to accelerate the folding process [45]. Some efforts have explored isothermal folding of DO; however, these approaches are generally structure-specific and require extensive screening to identify the precise folding temperature, which limits their broader applicability [35, 45, 46]. Given the increasing scope of DO in both research and applied settings, there is a growing need for faster and more generalizable folding protocols. This is especially relevant in fields where rapid production is crucial, such as therapeutic development, diagnostics, and high-throughput screening. In addition, faster and scalable folding methods would broaden the practical use of DNA nanostructures in areas such as sensing, plasmonics, lithography, surface functionalization, and programmable materials, where integration with devices and surfaces demands speed and scalability.

Here, we present an extensive analysis of the role of the temperature ramp in DO folding under various commonly used salt conditions and propose an alternative rapid-folding method that confines the annealing process to the 60°C–40°C range. We evaluated the folding behavior of four different complex 3D origami designs (Figures S1–S4): the 20-helix square box (20SB) based on a square lattice, the 24-helix bundle (24HB) based on a hexagonal lattice, the curved 13-helix ring (13R), and a functional two-state switchable cross-shaped structure (Cross) under standard Mg^{2+} salt conditions (Figure 1B). Additionally, we investigated the folding of the 20SB design under Na^{+} and $Choline^{+}$ conditions. The characterization of folding yield and structural uniformity was performed using agarose gel electrophoresis and atomic force microscopy (AFM). We report on the folding yield,

structural uniformity, and functionality, and compare the results with those obtained using the conventional 30 h stepwise annealing protocol. Notably, our findings reveal that folding yields tend to slowly plateau within the first 1–3 h, depending on the specific structure. We also observe that the functionality, e.g., the reconfigurability of the structures, is retained and remains unaffected. Importantly, we observe other benefits, such as reduced multimer formation in some instances, particularly with the 13R origami structure.

2 | Results and Discussions

2.1 | The 60–40 Folding Protocol

The most widely used protocols for folding DO involve gradually cooling the reaction from a high starting temperature (the melting temperature of DNA duplexes), typically around 80°C (or 65°C), down to room temperature (20°C). This stepwise annealing process, which spans a broad temperature range, generally takes 20–30 h to yield fully folded structures (Figure 1C). However, a key study by Sobczak et al. [45] demonstrated that the actual folding of DO occurs within a much narrower temperature window of approximately 4°C−5°C, which we refer to here as the 'ideal folding zone'. It was further shown that folding DO isothermally within this narrow window can result in some correctly folded structures within 30–60 min, depending on the design [45]. However, the ideal folding zone is structure-specific and therefore varies for different structures. As a result, developing an annealing protocol that targets only the ideal folding zone would require extensive screening and optimization for each structure, which is both time-consuming and resource-intensive. This makes such protocols impractical for general use, especially when studying or producing structures with multiple designs.

To address this, we investigated a modified folding protocol that focuses the annealing process within a broader but still constrained temperature range: 60°C to 40°C. This range was selected based on several literature reports indicating that the ideal folding zones of many DO structures lie within this range [34, 45, 47–49]. For example, in the study by Sobczak et al. [45], the folding of the platelike was observed between 60°C and 55°C, whereas the bricklike and gearlike structures folded between 55°C to 50°C. In this protocol, samples are first heated to 80°C for 15 min to ensure complete melting of DNA duplexes (same as standard 30 h stepwise protocol). The temperature is then rapidly reduced to 60°C, followed by a controlled, slow ramp from 60°C to 40°C, and finally a rapid drop to room temperature (20°C). We refer to this approach as the "60–40 ramp protocol". Importantly, we adjust the ramp rate within the 60°C–40°C segment, allowing the total time spent in this window to vary from as short as 5 min to as long as 5 h (Figure 1D). The goal of this annealing ramp is to focus folding within a temperature window that is broad enough to capture the ideal folding zones of diverse structures, while still enabling a substantial reduction in overall folding time.

To evaluate this protocol, we utilized the 20-helix Square Box (20SB) DO structure, which was folded in 1 × TE buffer with 15 mM Mg^{2+} with 10 nM scaffold and 100 nM staple concentrations. Initially, the 60–40 ramp was set for 30 min. As a control to verify the folding of the origami outside the 60–40 temperature zone, we folded two additional samples, one from 80°C to 60°C and the other from 40°C to 20°C. All samples were initially heated to 80°C for 15 min to denature any double-stranded DNA domains.

We used gel electrophoresis to characterize the structures and AFM for imaging the folded structures (Figure 1E,F). Gel electrophoresis results revealed that the 60–40 ramp resulted in a distinct, faster-migrating band, consistent with a well-folded, compact DO structure. In contrast, both control samples exhibited slower-migrating bands with smear and multimer formation, indicating the presence of misfolded or aggregated structures. These observations were confirmed by AFM imaging of the as-folded samples (without additional purification): the 60–40 sample showed a majority of correctly folded structures, whereas the 80–60 sample exhibited large DNA aggregates without recognizable features. The 40–20 sample also lacked well-formed structures but showed smaller aggregates and dense DNA clusters with dimensions similar to those of the target structure, suggesting incomplete folding.

Together, these results support the effectiveness of the 60–40 ramp protocol for a rapid folding of the 20SB DO structure. More importantly, they also indicate that, for this design, folding outside the 60°C−40°C range is not critical for origami structure formation. This observation is consistent with a recent study that reports successful folding within this same temperature window, although with a much slower 20 h ramp [34]. Nevertheless, for more complex multilayer origami or for multi-domain assemblies, restricting folding to 60°C–40°C may be less effective.

2.2 | 20SB

In this section, we investigate the effect of temperature ramp duration on DNA origami folding using the 60–40 ramp protocol described previously. The above-mentioned 20SB structure was folded in 1 × TE buffer containing 15 mM Mg^{2+}, with reaction times ranging from 5 min to 5 h: namely, 5, 10, 30 min, 1, 3, and 5 h. These samples were then compared to a reference sample folded using a typical 30 h stepwise annealing protocol. Folding outcomes were assessed using both gel electrophoresis and AFM with as-folded samples (i.e., without additional purification).

For relative quantitative comparison, gel electrophoresis images were first standardized (see Experimental Section) and then analyzed by integrating the intensity of each lane. The resulting integrated intensity plots are shown in Figure 2A. To estimate the yield of fully folded structures, we defined a reference region that fully encompasses the peak corresponding to the 30 h folded sample (assumed well folded DO structures). Using this reference region, we defined corresponding regions in all other samples at the same migration distance from the gel wells as the 30 h band (i.e., regions having the same electrophoretic mobility). We then calculated the area under the curve for all other samples within these defined regions, as illustrated in Figures 2A, S5 and S6. This can be simply thought of as considering (in the yield estimation) only the fraction of structures that have the same electrophoretic mobility as that of the well-folded 30 h samples. These calculated areas were then normalized by setting the 30 h sample to 100%, and the resulting relative yields (i.e., each sample's yield compared to the 30 h sample) were plotted in Figure 2B. This

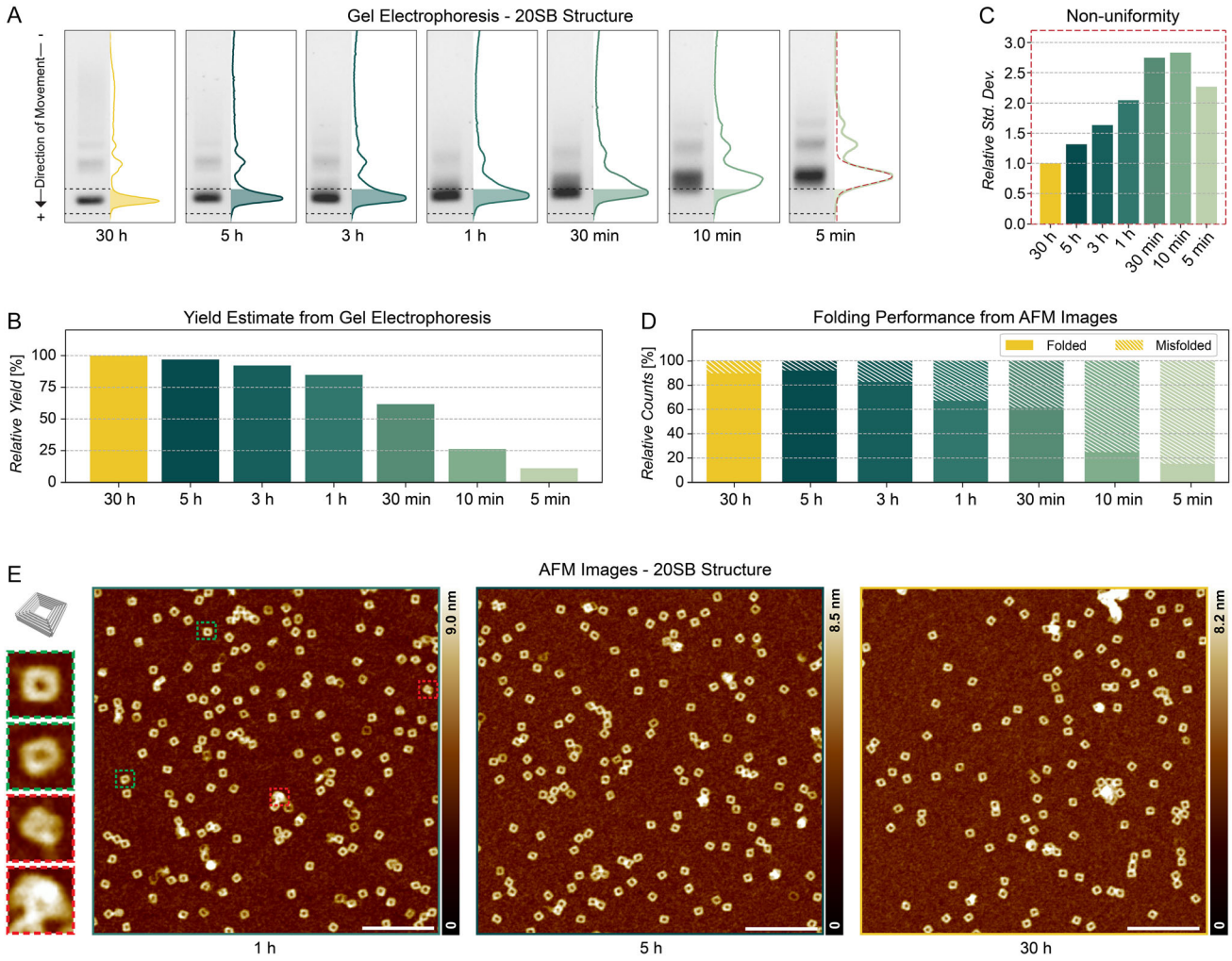

FIGURE 2 | The 60–40 folding of the 20SB DO structure. (A) Gel electrophoresis image with integrated intensity plots of samples folded for different reaction times. Gaussian fits of the intensity peaks, used to estimate peak spread, are shown in the rightmost panel. (B) Yield estimation plot based on integrated intensities from A. (C) Non-uniformity plot summarizing the relative standard deviation of the Gaussian-fitted peaks from A. (D) Folding performance for the 20 SB DO structure, highlighting the proportions of folded and misfolded structures across different folding times. (E) AFM images of unpurified samples folded for 1 and 5 h using the 60–40 protocol, compared to the 30 h control folded with the standard stepwise protocol. The zoomed-in images on the left highlight representative examples of folded (green) and misfolded (red) structures. Scale bars: 400 nm.

approach assumes that the 30 h band corresponds to well-folded DO structures and therefore measures the fraction of DO structures in other samples having the same electrophoretic mobility. However, it should be noted that alternative quantification methods, e.g., those based on light scattering [49, 50], or total double-stranded DNA concentration, or direct imaging, may result in slightly different yield estimates.

The relative yield plot (Figure 2B) clearly shows a rapid increase in folding yield from 5 min to 1 h, followed by a gradual plateauing beyond 1 h. Notably, the 1 h sample achieves nearly 80% of the yield of the 30 h control, whereas the 5 h sample achieves almost 95%, suggesting that the majority of folding can occur in a much shorter time when using the 60–40 ramp protocol. This represents a significant reduction in reaction time, accompanied by a marginal loss in the yield.

However, the yield alone does not fully capture the quality of the folded structures. To evaluate structural uniformity, we fitted Gaussian functions to the intensity peaks of each band (Figure 2A) and extracted the standard deviation (σ) of the fits as a measure of non-uniformity. These values were normalized and plotted in Figure 2C. The results show a slight but consistent increase in peak width for shorter folding times, indicating higher non-uniformity. This suggests that faster folding results in a broader distribution of structures—some fully folded, others partially folded—whereas longer reaction times produce more uniform assemblies.

To directly visualize the effectiveness of folding, we imaged the unpurified samples using AFM, as shown in Figures 2E and S7. Even at 5 min, the structures appear to have reached their intended approximate size, although the folding is incomplete as illustrated in Figure S7. By 1 h, a mixture with a majority of fully formed and some partially folded structures is observed (Figure 2E). However, by 5 h, the sample becomes almost indistinguishable from the 30 h sample (Figure 2E), demonstrating that high-quality folding can be achieved in one-sixth of the typical folding time. While the 5 h sample still shows slightly higher non-uniformity in gel analysis, this difference is subtle and barely distinguishable in the AFM images.

To quantify the observations from the AFM images, the numbers of fully folded and misfolded structures (including aggregates) were manually counted, as presented in Figure S12. For quantitative consistency, a total of 136, 165, 181, 175, 161, 156, and 90 structures were analyzed for the 30, 5, 3, 1 h, 30, 10, and 5 min samples, respectively. For this structure, the major distinguishing feature was the presence of a central hole: structures with an intact hole were classified as fully folded, whereas those lacking it were regarded as misfolded. Representative examples of fully folded and misfolded structures are highlighted in Figure 2E. The results are summarized in a normalized stacked bar plot in Figure 2D. The relative percentage of fully folded structures increases with reaction time but begins to plateau after approximately 3 h. Interestingly, the 5 h sample showed a slightly higher proportion of fully folded structures compared to the 30 h sample. While the difference is modest, the fact that the 5 h protocol is significantly faster yet still achieves superior folding efficiency underscores the potential of the 60–40 ramp. Additionally, the 30 h sample also displayed some degree of aggregation not observed in the other cases, which may account for its lower proportion of fully folded structures.

To further evaluate the versatility of the 60–40 ramp protocol, we performed the same set of folding experiments under magnesium-free conditions. The 20SB structure was folded using 1 × TE buffer supplemented with either 3 M NaCl or 3 M choline chloride, maintaining the same 60°C–40°C temperature ramp. The corresponding gel images, yield estimation, peak spread plots, and AFM images are shown in Figures 3, S8, and S9. The results closely resemble those obtained under typical magnesium conditions, suggesting that the protocol remains effective even in magnesium-free environments. Interestingly, in this case, we observe much higher yields for shorter folding times, such as 5 and 10 min (Figure 3B,F). This is also supported by the AFM images, where we observed several fully formed structures even at 10 min of folding, as shown in Figures S8 and S9.

Overall, these findings demonstrate that the 60–40 ramp protocol facilitates high-yield folding of the 20SB structure in a significantly reduced timeframe across multiple salt conditions. Although a trade-off in structural uniformity is observed at very short folding durations, as seen in Figures 2E, 3D,H, and S7–S9, the effect becomes minimal and almost indistinguishable beyond 1–3 h, as seen from the AFM images.

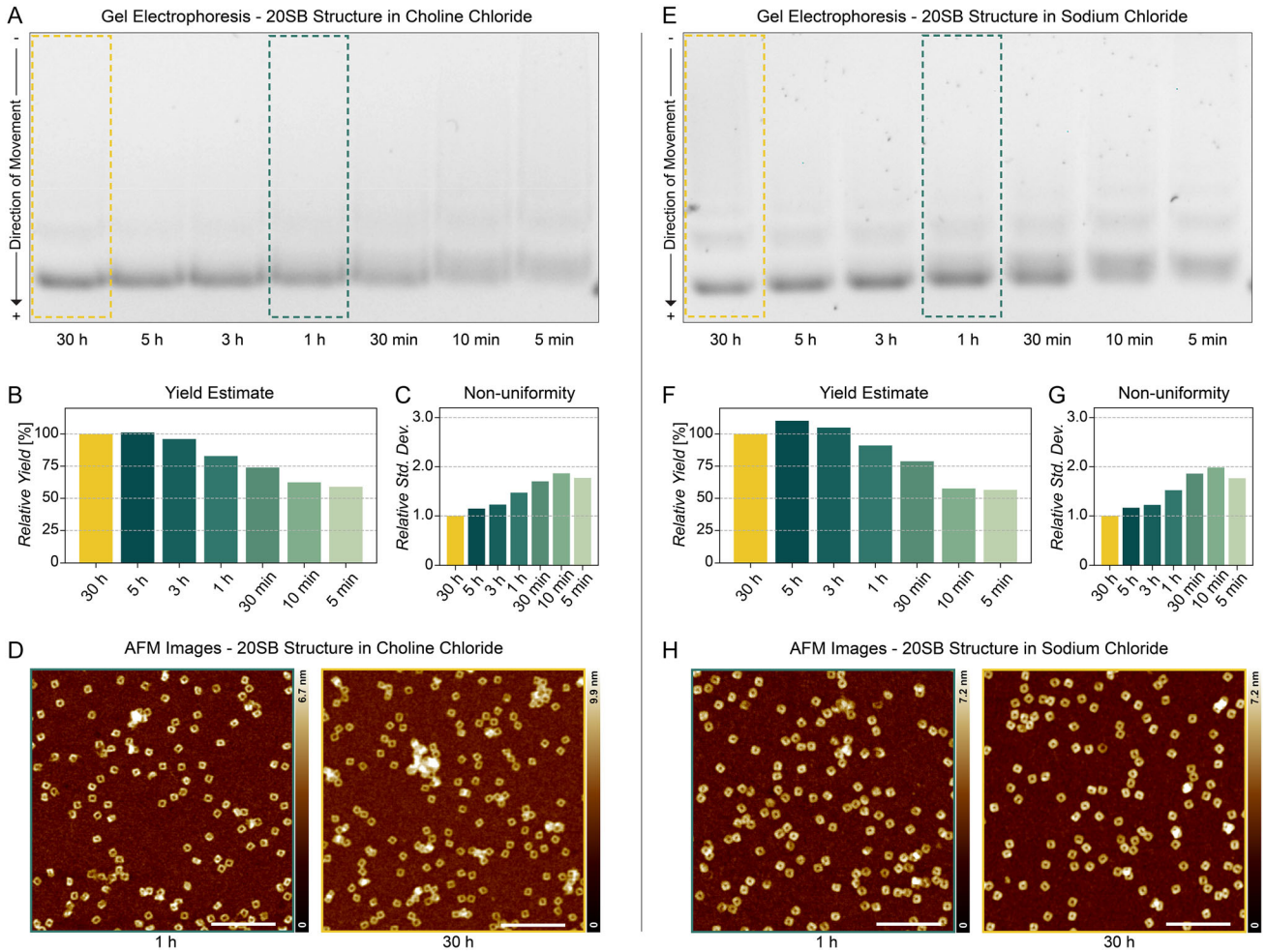

FIGURE 3 | Results for the 20SB structure folded in (A–D) 3 M choline chloride and (E–H) 3 M sodium chloride. (A,E) Gel electrophoresis images of 20SB samples folded at varying reaction times in (A) choline chloride and (E) sodium chloride. (B,F) Yield estimation plots derived from the integrated intensities of the gel bands. (C,G) Non-uniformity plots showing the relative standard deviation of the Gaussian-fitted peaks from the integrated intensity plots. (D,H) AFM images of unpurified samples folded for 1 h using the 60–40 protocol, compared with the 30 h control samples folded using the standard stepwise protocol. Scale bars: 400 nm.

2.3 | 24HB

We next applied the 60–40 ramp protocol to the 24-helix bundle (24HB) structure. The 24HB is a well-established DNA origami design, built on a hexagonal lattice, and widely used due to its rigidity and well-defined geometry [38, 51]. Folding was carried out under the same buffer conditions as before (1 × TE with 15 mM Mg^{2+}), with ramp durations ranging from 5 min to 5 h, alongside a 30 h stepwise protocol used as a control.

The gel electrophoresis results for the folding of 24HB are shown in Figure 4A. Compared to the 20SB structure, the 24HB exhibits significantly sharper and more compact bands, even at shorter folding times, suggesting that it folds more rapidly and uniformly. Quantitative analysis of the integrated band intensities (Figure 4B) reveals that approximately 85% of the 30 h yield is achieved in just 30 min, and over 95% yield is obtained by 3 h. Notably, the 5 h sample shows a slightly higher yield than the 30 h control, suggesting better folding during the shorter ramp.

The peak spread analysis, shown in Figure 4C, indicates minimal variation in structural uniformity across different folding times. While slightly broader peaks are observed for the shortest durations, the standard deviation remains low overall, especially beyond 30 min, suggesting that relatively homogeneous structures are obtained even with rapid folding.

AFM imaging, as shown in Figures 4D and S10, supports these observations. Well-formed 24HB structures appear as early as 10 min, and by 1 h, the structures are nearly indistinguishable from those folded for 30 h. The images reveal a clear transition from partially formed to fully folded structures within a significantly reduced time frame, with very little observable difference beyond 1 h.

These results highlight that the 24HB structure also folds efficiently and uniformly under the 60–40 ramp protocol. In this case, even very short folding times (10–30 min) produce high-yield, well-formed structures with nominal variation. This suggests that certain designs may be inherently more compatible with rapid folding strategies, further supporting the utility of the 60–40 protocol as a generalized, time-efficient folding approach.

2.4 | 13R

Following the analysis of the 24HB structure, we next examined the folding behavior of the 13-helix Ring (13R) structure, a

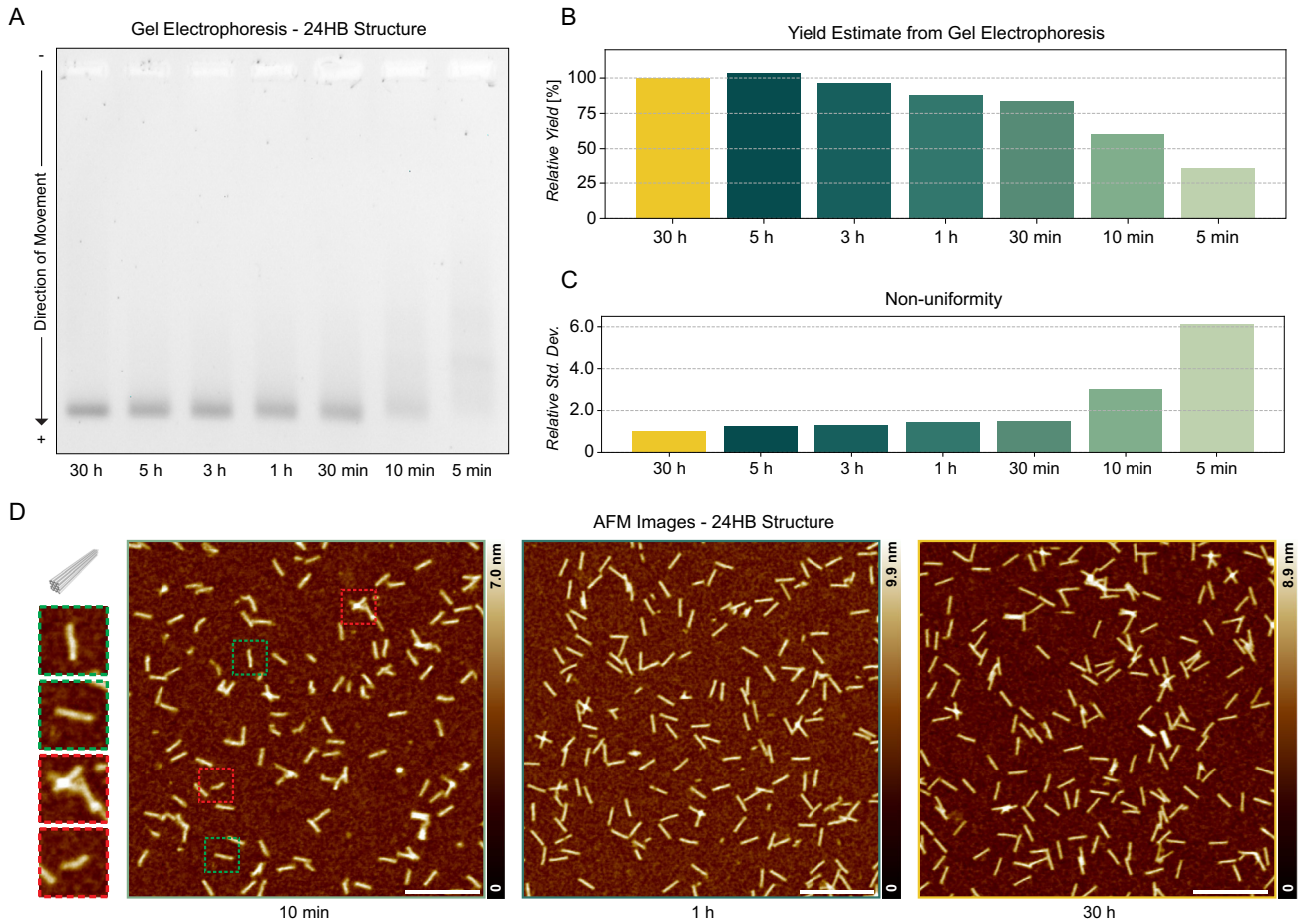

FIGURE 4 | The 60–40 folding of the 24HB DO structure. (A) Gel electrophoresis image of the 24HB DO structure for different folding times. (B) Yield estimation plot based on integrated intensities of the gel bands in A. (C) Non-uniformity plot summarizing the relative standard deviation of the Gaussian-fitted peaks to gel bands in A. (D) AFM images of the samples folded for 10 min and 1 h using the 60–40 protocol, compared to the 30 h control folded with the standard stepwise protocol. The zoomed-in images on the left highlight representative examples of folded (green) and misfolded (red) structures. Scale bars: 400 nm.

hexagonal lattice-based curved ring-shaped DNA origami design. This 13R structure tends to exhibit significant dimer and multimer formation when folded using the standard 30 h stepwise protocol [51, 52]. As with the previous structure, we applied the 60–40 ramp protocol, with folding durations ranging from 5 min to 5 h, and compared the results to the 30 h control. The gel images, yield estimations, and peak spread plots are shown in Figure 5A–C.

Importantly, the 13R structure displays a markedly different behavior compared to the previous two designs. For the 30 h control sample, a large fraction of the folded origami remained trapped in the gel wells, suggesting extensive aggregation and the presence of higher-order structures. This phenomenon is absent in all samples folded using the 60–40 ramp protocol, indicating that faster and more targeted folding may help reduce multimer formation and aggregation. As a result, the apparent yield of the 30 h sample is significantly lower, which is reflected in the yield estimation plot (Figure 5B). Notably, all the samples folded using the 60–40 protocol achieved higher yield compared to the 30 h control, and the yield increased steadily with folding time, reaching more than twice the yield of the 30 h protocol by 5 h. The peak spread analysis (Figure 5C) reveals a trend similar to that in earlier results, with slightly broader peaks at shorter folding durations, indicating slight non-uniformity, which decreases as the folding time increases. However, the magnitude of variation remains very low.

A particularly noteworthy observation emerges from the analysis of dimer-to-monomer ratios (Figure 5D). In samples folded using the 60–40 ramp for 3 and 5 h (samples with a clear dimer band), the dimer proportion is significantly lower compared to the 30 h control. Specifically, the 60–40 protocol yields approximately a 0.3 dimer-to-monomer ratio, whereas the 30 h sample exhibits a significantly higher ratio of 0.6. This suggests that the longer stepwise folding protocol may promote undesired dimerization and multimer formation. In contrast, the 60–40 protocol appears to favor monomeric folding pathways and reduce the likelihood of aggregation.

The 13R unpurified samples were also imaged using AFM (Figure 5F). Fully formed ring-like structures could be observed as early as the 5 min sample, see Figure S11, although most of

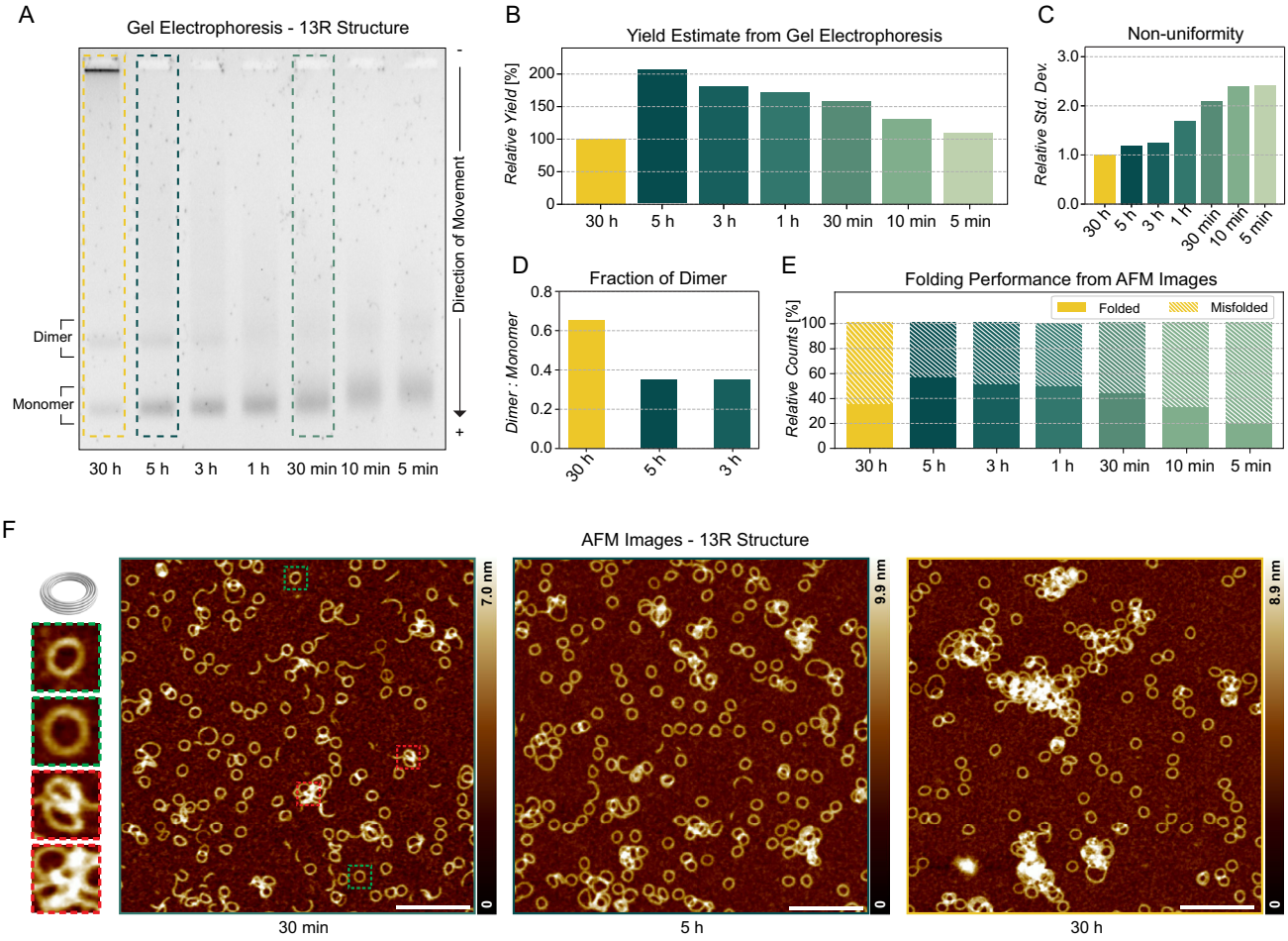

FIGURE 5 | The 60–40 folding of the 13R DO structure. (A) Gel electrophoresis image of the 13R DO structure for different folding times. (B) Yield estimation plot based on integrated intensities of the gel bands in A. (C) Non-uniformity plot summarizing the relative standard deviation of the Gaussian-fitted peaks to gel bands in A. (D) Plot of the ratio of integrated intensity of the dimer band to monomer band for 30 h (standard protocol), 5 h, and 3 h (60–40 protocol). (E) Folding performance for the 13R DO structure, highlighting the proportions of folded and misfolded structures across different folding times. (F) AFM images of the samples folded for 30 min and 5 h using the 60–40 protocol, compared to the 30 h control folded with the standard stepwise protocol. The zoomed-in images on the left highlight representative examples of folded (green) and misfolded (red) structures. Scale bars: 400 nm.

them appeared bent and not structurally intact. By 30 min (Figure 5F), a majority of the structures resembled the intended ring shape, alongside some partially folded "moon-like" shapes (rings that did not fully close). At 5 h, the sample contained more fully formed rings than the 30 h sample (Figure 5F). In the 30 h case, a large fraction of the structures was aggregated, consistent with the gel electrophoresis results, which led to a lower proportion of intact and usable 13R structures compared to the 1, 3, or 5 h samples.

To quantify these observations, the fully formed structures were manually counted from AFM images and summarized in Figures 5E and S13. A total of 269, 247, 273, 299, 222, 184, and 225 structures were examined for the 30, 5, 3, 1 h, 30, 10, and 5 min samples, respectively. Here, any unintended structures (e.g., dimers, multimers, aggregates, bent rings, or open rings) were classified as misfolded, while only uniform, closed-ring origami were considered fully folded (this definition contributed to the relatively higher fraction of misfolded structures across all samples in Figure 5E). Consistent with the gel electrophoresis results, the 60–40 protocol outperformed the conventional 30 h folding protocol, with the 5 h sample achieving nearly a 60% higher yield of fully folded structures. Shorter folding times tended to produce more open or bent rings, while longer folding times led to greater aggregation, as shown in Figure S11, particularly in the 30 h sample, which drastically reduced the number of usable 13R structures.

These findings suggest that prolonged folding may be counterproductive for aggregation-prone structures such as 13R. The

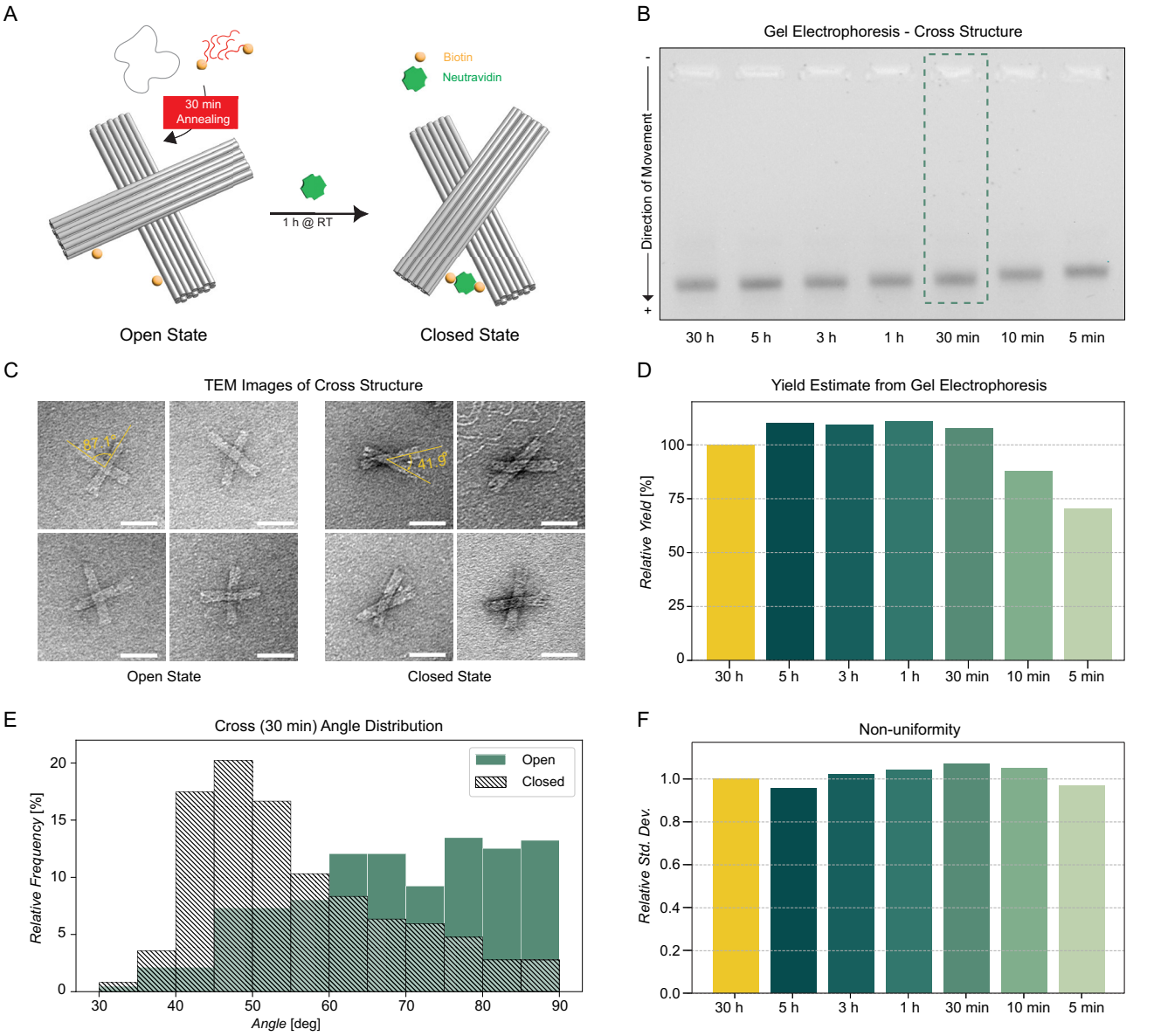

FIGURE 6 | The 60–40 folding of the Cross DO structure. (A) Schematic showing the switching of the Cross DO structure between open and closed states by the addition of Neutravidin. (B) Gel electrophoresis image of the Cross DO structure for different folding times. (C) TEM images of spin-purified samples, before (open) and after (closed) addition of Neutravidin. (D) Yield estimation plot based on integrated intensities of the gel bands in B. (E) Histogram of the measured angles for the open and closed state DO structures from the TEM images (Total structures analyzed – Open: 423, Closed: 252). (F) Non-uniformity plot summarizing the relative standard deviation of the Gaussian-fitted peaks to gel bands in B. Scale bars: 50 nm.

60–40 ramp not only enables faster and higher-yield folding but, more importantly, reduces misfolding and aggregation, highlighting its advantages for structurally complex or aggregation-prone designs.

2.5 | Cross

To evaluate how faster folding affects structural functionality, we investigated a Cross DNA origami structure. This design consists of two 14-helix bundles joined in a defined 3D orientation, with the dynamic property to transition between two distinct conformations—an open state and a closed state—in response to stimuli [21]. In our case, we assessed this functionality through biomolecular ligand binding. This serves as a critical test case, as it not only demonstrates the folding efficiency of the structure but also whether essential mechanical switching behavior in stimulus response is retained at shorter folding durations.

The Cross structure includes two modified staple strands functionalized with biotin at their 3′ end termini and a TT spacer (Figure 6A). After folding, these biotin moieties are positioned on adjacent arms of the origami and are designed to bind to Neutravidin (NA), as shown in Figure 6A. Upon addition of NA and incubation at room temperature for 1 h, the biotin–NA–biotin interaction drives the structural reconfiguration of the Cross from the open to the closed state (Figure 5A).

We applied the same experimental conditions (15 mM Mg^{2+}, 1 × TE buffer) and folding time series (5 min to 5 h, and 30 h control) as in previous experiments. This structure folded very well, as evidenced by the gel images (Figure 6B), which showed a sharp, distinct band even for short folding times (5–10 min), indicating efficient folding. Yield estimation and peak spread analysis (Figure 6D,F) confirm this observation: over 85% of the 30 h yield is reached within just 10 min, and by 30 min, the yield slightly exceeds that of the 30 h sample. Moreover, the standard deviation of the peaks remains low across all folding durations, indicating minimal structural heterogeneity (Figure 6F).

To assess whether the fast-folded structures retain switching functionality, we folded the Cross structure for just 30 min and then purified the folded samples using spin column filtration to remove excess staples. A subset of the folded structures was then incubated with Neutravidin to initiate the conformational switch. The samples were then imaged using transmission electron microscopy (TEM), and representative images of both open and closed states are shown in Figures 6C and S14–S17.

For quantitative comparison, we measured the angle between the arms of each Cross structure. Histograms of the measured angles (Figure 6E) reveal distinct distributions for the two conformational states: the open state shows a broader distribution peaking close to 90°, reflecting flexible arm orientation, while the closed state displays a much narrower peak centered around 45°−50°, consistent with the expected conformational constraint upon NA binding. These angle distributions closely agree with the Cross structure folded over 30 h, as shown in Figure S18, and previously reported values [10, 53–55], confirming that even rapidly folded structures maintain functional behavior.

Taken together, these results demonstrate that the 60–40 ramp protocol not only enables high-yield folding of the Cross structure in as little as 30 min but also preserves structural reconfigurability. This highlights a key point that, despite having slightly higher non-uniformity at shorter folding times, functional performance is not compromised. This further supports the general usability of rapid folding approaches for practical applications.

3 | Conclusion

In this study, we examined the role of temperature ramp in the folding of DNA origami nanostructures using a modified version of the standard stepwise protocol. By restricting the annealing process to a narrower yet sufficiently broad temperature window between 60°C and 40°C, we were able to significantly reduce the folding time without heavily compromising yield or structural quality. Comparative experiments on folding between 80°C–60°C and 40°C–20°C reinforced the conclusion that the majority of folding occurs specifically within this 60°C–40°C window, suggesting that this window captures the ideal folding conditions for a variety of DO designs.

A detailed analysis of various structural types, including square lattice structures, hexagonal lattice structures, curved structures, and switchable functional structures, was conducted. It revealed that folding is typically very rapid, and high yields can be achieved in a fraction of the time required by conventional 30 h stepwise protocols. While faster-folded samples did show slightly higher non-uniformity, the differences were small. For most structures, samples folded for just 3 h were indistinguishable from those folded for 30 h, even by AFM imaging. The protocol also performed well in magnesium-free conditions with salts like NaCl and choline chloride. In some cases, such as the 13R structure, the shorter ramp protocol not only enabled faster folding but, more importantly, led to reduced aggregation and multimer formation, resulting in a higher proportion of monomeric structures. With the Cross structure, we found that even structures folded for as little as 30 min retained their intended function of conformational switching between two states as effectively as those folded over more extended periods, indicating that minor structural non-uniformity does not necessarily compromise overall functionality.

Overall, this work aims to contribute to a better understanding of the temperature dependance of DO folding—an aspect that remains relatively underexplored. It also suggests a more general and time-efficient folding protocol that may be particularly valuable for applications where high-throughput screening of multiple designs is needed, or where extremely high folding yield is not critical. Notably, the structures tested here were pre-existing designs folded under commonly used conditions, without extensive optimization, which highlights the broad applicability and practicality of the proposed 60°C–40°C protocol. Further tuning of the ramp rate or narrowing of the folding window for individual structures could yield even better results, especially when folding requirements are stricter.

This protocol does not aim to replace conventional stepwise folding altogether but instead provides an effective and more accessible alternative for rapid prototyping, large-scale studies, or use in automated and high-throughput settings. With further refinement, it may serve as a flexible framework for the accelerated and reliable preparation of a wide variety of DNA origami structures.

4 | Experimental Section

4.1 | DNA Origami Assembly

The DNA single-stranded M13-based scaffolds with lengths 8064 bases (p8064, for 20SB), 7560 bases (p7560, for 24HB and Cross), and 7249 bases (p7249, for 13R) were purchased from Tilibit Nanosystems. The staple strands were obtained from IDT. For the scaffold (10 nM), a tenfold excess of each staple (100 nM) was used for origami folding. The DNA origami templates were designed using caDNAno software [56]. The strand routing diagram for all the structures can be found in Figures S1–S4.

4.2 | Agarose Gel Electrophoresis

For gel electrophoresis, 1% agarose gels (Invitrogen UltraPure Agarose, Fisher Scientific) were prepared and stained with 1 × SYBR safe DNA gel stain (Fisher Scientific). As a running buffer, 0.5 × TBE (sterile-filtered solution of Tris (1 M), boric acid (0.9 M), and EDTA (0.01 M), from Fisher Scientific) with magnesium chloride (13 mM) was used. The samples were loaded into the gel with loading dye containing Bromophenol blue (0.25%) and Ficoll 400 (15%). Results were imaged using a Bio-Rad Molecular Imager Gel Doc XR System and analyzed with Image Lab and ImageJ software.

4.3 | Gel Electrophoresis Image Analysis

The gel electrophoresis images were corrected for misalignment and adjusted to ensure that the gel bands ran straight by applying transformations and perspective correction, setting the gel wells and staple bands horizontal and parallel. This step accounted for gel-box- or equipment-specific errors in band mobility. The images were then scaled and cropped, after which the integrated density plots and other analyses were performed in Python.

4.4 | Spin Column Purification

Spin-filter purification of the Cross structures was carried out using centrifugal filter units (Merck Amicon Ultra-0.5, Merck, 100 kDa MWCO). Samples were centrifuged at 4000 relative centrifugal force (rcf) for 4 min, and the process was repeated three times to remove excess staples. During filtration, the buffer was kept the same as the folding buffer. The final concentration of the DO after purification was estimated using a UV–vis spectrophotometer (BioSpectrometer, Eppendorf).

4.5 | TEM Sample Preparation and Imaging

The spin-purified samples were drop-cast on plasma-cleaned TEM grids and incubated for 10–15 min at room temperature. Then, the excess sample was removed, and a Uranyl Formate solution (0.75%) was deposited on the TEM grids for 30 s before blotting the excess off with filter paper. The samples were then left to dry in air for a few minutes before imaging. The images were taken using FEI Tecnai 12 (120 kV TEM).

4.6 | AFM Sample Preparation and Imaging

The samples were imaged on Si substrates coated with a layer of poly-L-lysine (PLL). Initially, the substrates were plasma-cleaned at 75 W (TG100, PIE Scientific) for 2 min with a mixture of air (10 sccm) and water (10 sccm). The Si chips were then dip-coated in a PLL solution containing PLL (0.01%, $M_W \approx 1\,50\,300$ k g mol^{-1}, Merck), Tris (10 mM, $M_W \approx 121.14$ g mol^{-1}, Sigma), and NaCl (50 mM) for 2 min, and rinsed afterward with Type-1 water and dried using nitrogen gas. The substrates were baked in a lab oven (Heratherm General Protocol Oven, Thermo Fisher Scientific) for 10 min at 60°C to remove absorbed water, resulting in a flatter imaging surface (sufficient time should be given for the substrates to cool down afterward). Finally, the DNA origami solution (≈2.5 nM) was deposited for 2 min before being gently rinsed with a buffer (0.5 × TBE, 11 mM $MgCl_2$), followed by Type-1 water and drying with nitrogen gas. The samples were imaged using ScanAsyst mode AFM (Dimension Icon, Bruker) with aluminum-coated probes (Tap150Al-G, Budget Sensors). The AFM images were taken at a scan rate of 1 Hz with *x*- and *y*-sampling of 512 points and a scan size of 2 μm. All the AFM data were processed using (NanoScope Analysis 3.0).

Author Contributions

Anurit Dey: conceptualization (equal), investigation (lead), methodology (lead), validation (lead), visualization (lead), writing – original draft (lead), writing – review and editing (lead). **Mohammed Mustafa A. Al Hussain**: investigation (equal), methodology (equal), validation (equal), visualization (supporting), writing – original draft (supporting), writing – review and editing (equal). **Xuan-Hung Pham**: investigation (supporting), methodology (supporting), supervision (supporting), validation (supporting), writing – original draft (supporting), writing – review and editing (supporting). **Jacky Loo**: methodology (supporting), validation (supporting), writing – original draft (supporting), writing – review and editing (supporting). **Ashwin Karthick Natarajan**: methodology (supporting), writing – review and editing (supporting). **Anton Kuzyk**: conceptualization (lead), funding acquisition (lead), project administration (lead), supervision (lead), writing – original draft (equal), writing – review and editing (equal).

Acknowledgments

This work was supported by the Research Council of Finland (grant 362134), the European Research Council (ERC CoG grant EDRIVE, 101045516), the Research Council of Finland Flagship Programme, Photonics Research and Innovation (PREIN), decision number 346529, Aalto University and the Finnish Ministry of Education and Culture through the PREIN/I-DEEP doctoral pilot (VN/3137/2024-OKM-4). A.K.N. acknowledges the financial support from Alexander von Humboldt Research Fellowship and Marie Skłodowska-Curie Actions Individual Fellowship grant agreement number 101150838 ("DNA-MolScaff"). The authors acknowledge the provision of facilities and technical support by Aalto University at OtaNano – Nanomicroscopy Center (Aalto-NMC) and OtaNano – Micronova Nanofabrication Centre. The authors thank Luis García García-Arisco for help with TEM, Vu Hoang Nguyen for assistance with the design of DNA origami structures, and Dr. Pierre Bléteau for the helpful discussions.

Open access publishing facilitated by Aalto-yliopisto, as part of the Wiley - FinELib agreement.

Funding

This work was supported by the Research Council of Finland (Grant: 362134); the European Research Council (Grant: ERC CoG grant

EDRIVE, 101045516); the Research Council of Finland Flagship Programme, Photonics Research and Innovation (PREIN), Aalto University (Grant: 346529); the Alexander von Humboldt Research Fellowship and Marie Skłodowska-Curie Actions Individual Fellowship grant agreement number 101150838 ("DNA-MolScaff"); and the PREIN/I-DEEP doctoral pilot program, Finnish Ministry of Education and Culture (Grant: VN/3137/2024-OKM-4).

Conflicts of Interest

The authors declare no conflicts of interest.

Data Availability Statement

The data that support the findings of this study are available from the corresponding author upon reasonable request.

References

1. N. C. Seeman and A. M. Belcher, "Emulating Biology: Building Nanostructures from the Bottom Up," *Proceedings of the National Academy of Sciences* 99 (2002): 6451.

2. N. C. Seeman, "DNA in a Material World," *Nature* 421 (2003): 427.

3. N. C. Seeman and H. F. Sleiman, "DNA Nanotechnology," *Nature Reviews Materials* 3 (2017): 17068.

4. C. E. Castro, F. Kilchherr, D.-N. Kim, et al., "A Primer to Scaffolded DNA Origami," *Nature Methods* 8 (2011): 221.

5. S. Dey, C. H. Fan, K. Gothelf, et al., "DNA Origami," *Nature Reviews Methods Primers* 1 (2021): 13, https://doi.org/10.1038/s43586-020-00009-8.

6. P. W. K. Rothemund, "Folding DNA to Create Nanoscale Shapes and Patterns," *Nature* 440 (2006): 297.

7. D. Jiang, Z. Ge, H.-J. Im, et al., "DNA Origami Nanostructures Can Exhibit Preferential Renal Uptake and Alleviate Acute Kidney Injury," *Nature Biomedical Engineering* 2 (2018): 865.

8. Q. Zhang, Q. Jiang, N. Li, et al., "DNA Origami as an Drug Delivery Vehicle for Cancer Therapy," *ACS Nano* 8 (2014): 6633.

9. Q. Jiang, S. Liu, J. Liu, Z.-G. Wang, and B. Ding, "Rationally Designed DNA-Origami Nanomaterials for Drug Delivery In Vivo," *Advanced Materials* 31 (2019): 1804785.

10. Y. Huang, M.-K. Nguyen, A. K. Natarajan, V. H. Nguyen, and A. Kuzyk, "A DNA Origami-Based Chiral Plasmonic Sensing Device," *ACS Applied Materials & Interfaces* 10 (2018): 44221.

11. M. Raveendran, A. J. Lee, R. Sharma, C. Wälti, and P. Actis, "Rational Design of DNA Nanostructures for Single Molecule Biosensing," *Nature Communications* 11 (2020): 4384.

12. M. Dass, F. N. Gür, K. Kołątaj, M. J. Urban, and T. Liedl, "DNA Origami-Enabled Plasmonic Sensing," *The Journal of Physical Chemistry C* 125 (2021): 5969.

13. N. Liu and T. Liedl, "DNA-Assembled Advanced Plasmonic Architectures," *Chemical Reviews* 118 (2018): 3032.

14. A. Kuzyk, R. Jungmann, G. P. Acuna, and N. Liu, "DNA Origami Route for Nanophotonics," *ACS Photonics* 5 (2018): 1151.

15. J. Lee, J. Kim, G. Posnjak, et al., "DNA Origami Colloidal Crystals: Opportunities and Challenges," *Nano Letters* 25 (2025): 16.

16. K. Tapio, C. Kielar, J. M. Parikka, et al., "Large-Scale Formation of DNA Origami Lattices on Silicon," *Chemistry of Materials: A Publication of the American Chemical Society* 35 (2023): 1961.

17. Y. Xin, B. Shen, M. A. Kostiainen, et al., "Scaling Up DNA Origami Lattice Assembly," *Chemistry – A European Journal* 27 (2021): 8564.

18. S. H. Park, J. Lee, C. Kim, B. Kang, A. Gopinath, and S. Lee, "Selective Binding of DNA Origami on Self-Assembled Monolayer-Patterned Gold Substrate," *ACS Materials Letters* 7 (2025): 2565.

19. M. J. Urban, P. K. Dutta, P. Wang, et al., "Plasmonic Toroidal Metamolecules Assembled by DNA Origami," *Journal of the American Chemical Society* 138 (2016): 5495.

20. P. Wang, J.-H. Huh, J. Lee, et al., "Magnetic Plasmon Networks Programmed by Molecular Self-Assembly," *Advanced Materials* 31 (2019): 1901364.

21. A. Kuzyk, R. Schreiber, H. Zhang, A. O. Govorov, T. Liedl, and N. Liu, "Reconfigurable 3D Plasmonic Metamolecules," *Nature Materials* 13 (2014): 862.

22. S. Li, Q. Jiang, S. Liu, et al., "A DNA Nanorobot Functions as a Cancer Therapeutic in Response to a Molecular Trigger In Vivo," *Nature Biotechnology* 36 (2018): 258.

23. J. Chao, J. Wang, F. Wang, et al., "Solving Mazes with Single-Molecule DNA Navigators," *Nature Materials* 18 (2019): 273.

24. A. J. Thubagere, W. Li, R. F. Johnson, et al., "A Cargo-Sorting DNA Robot," *Science* 357 (2017): eaan6558.

25. L. Ding, B. Liu, A. Peil, S. Fan, J. Chao, and N. Liu, "DNA-Directed Assembly of Photonic Nanomaterials for Diagnostic and Therapeutic Applications," *Advanced Materials* 37 (2025): 2500086.

26. G. Posnjak, X. Yin, P. Butler, et al., "Diamond-Lattice Photonic Crystals Assembled from DNA Origami," *Science* 384 (2024): 781–785, https://doi.org/10.1126/science.adl2733.

27. H. Liu, M. Matthies, J. Russo, et al., "Inverse Design of a Pyrochlore Lattice of DNA Origami through Model-Driven Experiments," *Science* 384 (2024): 776.

28. P. W. Majewski, A. Michelson, M. A. L. Cordeiro, et al., "Resilient Three-Dimensional Ordered Architectures Assembled from Nanoparticles by DNA," *Science Advances* 7 (2021): eabf0617.

29. J. S. Kahn, B. Minevich, A. Michelson, et al., "Encoding Hierarchical 3D Architecture through Inverse Design of Programmable Bonds," *Nature Materials* 24 (2025): 1273.

30. L. Song, Q. Jiang, Z.-G. Wang, and B. Ding, "Self-Assembled DNA Nanostructures for Biomedical Applications," *ChemNanoMat* 3 (2017): 713.

31. P. Zhan, A. Peil, Q. Jiang, et al., "*Recent Advances in DNA Origami-Engineered Nanomaterials and Applications*," *Chemical Reviews* 123, no. 7 (2023): 3976–4050, https://doi.org/10.1021/acs.chemrev.3c00028.

32. S. M. Douglas, H. Dietz, T. Liedl, B. Högberg, F. Graf, and W. M. Shih, "Self-Assembly of DNA into Nanoscale Three-Dimensional Shapes," *Nature* 459 (2009): 414.

33. Y. Ke, S. M. Douglas, M. Liu, et al., "Multilayer DNA Origami Packed on a Square Lattice," *Journal of the American Chemical Society* 131 (2009): 15903.

34. T. Aksel, E. J. Navarro, N. Fong, and S. M. Douglas, "Design Principles for Accurate Folding of DNA Origami," *Proceedings of the National Academy of Sciences of the United States of America* 121 (2024): e2406769121, https://doi.org/10.1073/pnas.2406769121.

35. F. Schneider, N. Möritz, and H. Dietz, "The Sequence of Events during Folding of a DNA Origami," *Science Advances* 5 (2019): eaaw1412.

36. S. Gambietz, L. J. Stenke, and B. Saccà, "Sequence-Dependent Folding of Monolayered DNA Origami Domains," *Nanoscale* 15 (2023): 13120–13132.

37. A. Chandran, D. Ghoshdastidar, and S. Senapati, "Groove Binding Mechanism of Ionic Liquids: A Key Factor in Long-Term Stability of DNA in Hydrated Ionic Liquids?," *Journal of the American Chemical Society* 134 (2012): 20330.

38. T. G. Martin and H. Dietz, "Magnesium-Free Self-Assembly of Multi-Layer DNA Objects," *Nature Communications* 3 (2012): 1103.

39. M. Nakano, H. Tateishi-Karimata, S. Tanaka, and N. Sugimoto, "Choline Ion Interactions with DNA Atoms Explain Unique Stabilization of A–T Base Pairs in DNA Duplexes: A Microscopic View," *The Journal of Physical Chemistry B* 118 (2014): 379.

40. A. Rodriguez, B. R. Madhanagopal, K. Sarkar, et al., "Counterions Influence the Isothermal Self-Assembly of DNA Nanostructures," *Science Advances* 11 (2025): eadu7366.

41. Z. Sun, Y. Shen, W. Wang, and B. Wei, "DNA Self-Assembly Optimization by Betaine and its Analogs," *Small* 20 (2024): 2400930.

42. R. Vijayaraghavan, A. Izgorodin, V. Ganesh, M. Surianarayanan, and D. R. MacFarlane, "Long-Term Structural and Chemical Stability of DNA in Hydrated Ionic Liquids," *Angewandte Chemie, International Edition* 49 (2010): 1631.

43. I. Gállego, M. A. Grover, and N. V. Hud, "Folding and Imaging of DNA Nanostructures in Anhydrous and Hydrated Deep-Eutectic Solvents," *Angewandte Chemie, International Edition* 54 (2015): 6765.

44. C. Kielar, Y. Xin, B. Shen, et al., "On the Stability of DNA Origami Nanostructures in Low-Magnesium Buffers," *Angewandte Chemie, International Edition* 57 (2018): 9470.

45. J. P. J. Sobczak, T. G. Martin, T. Gerling, and H. Dietz, "Rapid Folding of DNA into Nanoscale Shapes at Constant Temperature," *Science* 338 (2012): 1458.

46. C. Rossi-Gendron, F. El Fakih, L. Bourdon, et al., "Isothermal Self-Assembly of Multicomponent and Evolutive DNA Nanostructures," *Nature Nanotechnology* 18 (2023): 1311.

47. A. Kopielski, A. Schneider, A. Csáki, and W. Fritzsche, "Isothermal DNA Origami Folding: Avoiding Denaturing Conditions for One-Pot, Hybrid-Component Annealing," *Nanoscale* 7 (2015): 2102.

48. J. L. T. Wah, C. David, S. Rudiuk, D. Baigl, and Aé Estevez-Torres, "Observing and Controlling the Folding Pathway of DNA Origami at the Nanoscale," *ACS Nano* 10 (2016): 1978.

49. H. Ijäs, T. Liedl, V. Linko, and G. Posnjak, "A Label-Free Light-Scattering Method to Resolve Assembly and Disassembly of DNA Nanostructures," *Biophysical Journal* 121 (2022): 4800.

50. Q. Zhang, X. Chang, A. Ebrahimimojarad, A. Shah, F. Zhang, and J. Fu, "Analyzing DNA Origami Nanostructure Assembly by Dynamic Light Scattering and Nanoparticle Tracking Analysis," *Small Methods* 9 (2025): 2500295.

51. M.-K. Nguyen, V. H. Nguyen, A. K. Natarajan, et al., "Ultrathin Silica Coating of DNA Origami Nanostructures," *Chemistry of Materials* 32 (2020): 6657.

52. H. Nguyen, "*Design, Assembly and Characterization of Highly Curved DNA Origami Structures*" (MSc Thesis, Aalto University, 2019).

53. A. K. Natarajan, J. Ryssy, and A. Kuzyk, "A DNA Origami-Based Device for Investigating DNA Bending Proteins by Transmission Electron Microscopy," *Nanoscale* 15 (2023): 3212.

54. A. Kuzyk, Y. Yang, X. Duan, et al., "A Light-Driven Three-Dimensional Plasmonic Nanosystem that Translates Molecular Motion into Reversible Chiroptical Function," *Nature Communications* 7 (2016): 10591.

55. J. Ryssy, A. K. Natarajan, J. Wang, et al., "Light-Responsive Dynamic DNA-Origami-Based Plasmonic Assemblies," *Angewandte Chemie, International Edition* 60 (2021): 5859.

56. S. M. Douglas, A. H. Marblestone, S. Teerapittayanon, A. Vazquez, G. M. Church, and W. M. Shih, "Rapid Prototyping of 3D DNA-Origami Shapes with caDNAno," *Nucleic Acids Research* 37 (2009): 5001.

Supporting Information

Additional supporting information can be found online in the Supporting Information section. **Supporting Fig. S1:** Strand routing diagram of the 20SB DNA origami structure. **Supporting Fig. S2:** Strand routing diagram of the 24HB DNA origami structure. **Supporting Fig. S3:** Strand routing diagram of the 13R DNA origami structure. **Supporting Fig. S4:** Strand routing diagram of the Cross DNA origami structure. **Supporting Fig. S5: Gel Image Analysis**. The raw gel images were cropped into individual bands, and a simple first-degree polynomial background correction was applied. To estimate yield, we defined a region encompassing the entire peak corresponding to the 30 h sample (as shown here). The area under the curve within this region was calculated, providing a measure of yield. Each peak was then fitted with a Gaussian function, and the standard deviation (σ) obtained from the fit was used to quantify peak spread, serving as a measure of structural non-uniformity. **Supporting Fig. S6:** An example of the gel image analysis applied to all bands of a given structure. The 30 h sample region was used as a reference, and corresponding regions were defined for all other samples at the same vertical level. The area under the curve within this region was then calculated for each sample to estimate yield. A Gaussian peak fit was applied to all intensity curves, and the standard deviation (σ) extracted from the fit parameters was used to quantify peak spread, providing a measure of structural non-uniformity. **Supporting Fig. S7: AFM images of the 20SB structure folded in 15 mM Mg^{2+} and 1 × TE buffer**. The 30 h sample was folded using the standard stepwise protocol, while all other samples were folded using the 60–40 protocol, with the total folding time indicated below each image. Even when samples were folded for 5 min, some fully formed structures were observed, along with the majority of DNA clusters of about the same size as the fully formed structures. The number of fully formed structures increases with the increase in folding time. Scale bars: 400 nm. **Supporting Fig. S8: AFM images of the 20SB structure folded in 3 M Choline$^+$ and 1 × TE buffer**. The 30 h sample was folded using the standard stepwise protocol, while all other samples were folded using the 60–40 protocol, with the total folding time indicated below each image. Here, samples folded for 5 or 10 min have a higher number of fully formed structures compared to the 20SB structures folded in 15 mM Mg^{2+} (Figure S7). However, for longer folding times, the behavior is very similar in both conditions. The number of fully formed structures increases with the increase in folding time. Scale bars: 400 nm. **Supporting Fig. S9: AFM images of the 20SB structure folded in 3 M Na^+ and 1 × TE buffer**. The 30 h sample was folded using the standard stepwise protocol, while all other samples were folded using the 60–40 protocol, with the total folding time indicated below each image. Similar to the results in Figure S8, samples folded for 5 or 10 min also have a higher number of fully formed structures compared to the structures in Figure S7. There is no significant difference in the folding behavior for longer folding times. The number of fully formed structures increases with the increase in folding time. Scale bars: 400 nm. **Supporting Fig. S10: AFM images of the 24HB structure folded in 15 mM Mg^{2+} and 1 × TE buffer**. The 30 h sample was folded using the standard stepwise protocol, while all other samples were folded using the 60–40 protocol, with the total folding time indicated below each image. In this case, the structural defects are not easily noticeable (the 10 min sample looks very close to the 30 h sample in terms of proper folding). However, the 10 min sample has broken/partially folded origami. The number of fully formed structures increases with the increase in folding time. Scale bars: 400 nm. **Supporting Fig. S11: AFM images of the 13R structure folded in 15 mM Mg^{2+} and 1 × TE buffer**. The 30 h sample was folded using the standard stepwise protocol, while all other samples were folded using the 60–40 protocol, with the total folding time indicated below each image. Here, it can be clearly seen that higher folding times result in more multimers and aggregates. The shorter folding time samples exhibit a high number of partially folded, broken ring structures, but they tend to form fewer aggregates. Scale bars: 400 nm. **Supporting Fig. S12: Calculation of the folding performance for the 20SB structure**. The structures marked with green are considered fully folded, and the structures marked with red are considered misfolded. The structures that are either overlapping or on the edges, where it is difficult to categorize them as either folded or misfolded, are marked in yellow and are not considered in the calculations. Scale bars: 400 nm. **Supporting Fig. S13: Calculation of the folding performance for the 13R structure**. This structure tends to form numerous multimers and aggregates. Hence,

only the intended monomeric structures are marked with green and are considered as fully folded. All other structures, including dimers, multimers, aggregates, partially folded, broken moon-like structures, are marked in red and considered misfolded. The structures on the edges, where it is difficult to categorize them as either folded or misfolded, are not considered in the calculations. Scale bar: 400 nm. **Supporting Fig. S14:** TEM images of the spin-purified Cross structure folded for 30 min using the 60-40 protocol in open state (i.e., before addition of Neutravidin). **Supporting Fig. S15:** TEM images of the spin-purified Cross structure folded for 30 min using the 60-40 protocol in the closed state. The structures were incubated with Neutravidin for 1 h at room temperature to induce switching to the closed state before imaging. **Supporting Fig. S16:** TEM images of the spin-purified Cross structure folded for 30 h using the standard protocol in the open state (i.e., before addition of Neutravidin). **Supporting Fig. S17:** TEM images of the spin-purified Cross structure folded for 30 h using the standard protocol in the closed state. The structures were incubated with Neutravidin for 1 h at room temperature to induce switching to the closed state before imaging. **Supporting Fig. S18:** Histogram of the angles of the Cross structure folded for 30 h in the open state and closed state. (Total structures analyzed – Open: 377, Closed: 414).